



Near surface structure of Sodankylä area in Finland, obtained by advanced method of passive seismic interferometry

Nikita Afonin^{1,5}, Elena Kozlovskaya^{1,2,4}, Suvi Heinonen², Stefan Buske³

¹Oulu Mining School, POB-3000, FIN-90014, University of Oulu, Finland

5 ²Geological Survey of Finland, P.O. Box 96, FI-02151, Espoo, Finland

³TU Bergakademie Freiberg, Institute of Geophysics and Geoinformatics, Freiberg, Germany

⁴Sodankylä Geophysical Observatory, University of Oulu, Finland

⁵N. Laverov Federal Center for Integrated Arctic Research of the Ural Branch of the Russian Academy of Sciences, Arkhangelsk, Russia

10

Correspondence to: Nikita Afonin (nikita.afonin@oulu.fi)

Abstract. Controlled-source seismic exploration surveys are not always possible in nature-protected areas. As an alternative, application of passive seismic techniques in such areas can be proposed. In our study, we show results of passive seismic interferometry application for mapping the uppermost crust in the area of active mineral exploration in Northern Finland. We are utilizing continuous seismic data acquired by **Sercel Unite Wireless multichannel recording system** along several profiles during XSoDEx (eXperiment of SOdankylä Deep Exploration) project. The objective of the project was to obtain a structural image of the upper crust in the Sodankylä area of Northern Finland in order to achieve a better understanding of the mineral system at depth. The key experiment of the project was a high-resolution seismic reflection experiment, and continuous passive seismic data was acquired in parallel with reflection seismic data acquisition. Due to this, the length of passive data suitable for noise cross-correlation was limited to several hours. In addition, analysis of the passive data demonstrated that dominating sources of ambient noise are non-stationary and have different origin across the XSoDEx study area. As the long data registration period and isotropic azimuthal distribution of noise sources are two major conditions for diffuse wavefield necessary for Empirical Green's Functions (EGFs) extraction, the conventional techniques of passive seismic interferometry was not possible to apply. To find the way to obtain EGFs, we used numerical modelling to investigate the properties of seismic noise originating from sources with different characteristics and propagating inside synthetic heterogeneous Earth models that models real geological conditions in the XSoDEx study area. The modelling demonstrated that scattering of ballistic waves on irregular shape heterogeneities, such as massive sulphides or mafic intrusions, could produce diffused wavefield composed mainly of scattered surface waves. This scattered wavefield can be used to retrieve reliable Empirical Green Functions (EGFs) from short-term and non-stationary data, using a special technique called "signal-to-noise ratio stacking" (SNRS). The EGFs calculated for the XSoDEx profiles were inverted in order to obtain S-wave velocity models down to the depth of 300 meters. The obtained velocity models agree well with geological data and complement the results of reflection seismic data interpretation.

25
30



1 Introduction

Exploration of new mineral deposits is an actual task because the modern world needs many types of minerals for functioning (Reid, 2011). Most of the shallow mineral deposits around the world nowadays are well known and exploration of new deep mineral deposits becomes more difficult than earlier (Vasara, 2018). That is why the cost-effectiveness of exploration also decrease. Moreover, there is the problem that application of controlled-source seismic exploration is not always possible in nature-protected areas. Particularly in the Arctic areas, non-invasive, environmentally friendly exploration is relevant. As an alternative, application of passive seismic techniques in such areas has been proposed. The main advantage of passive seismic methods is possibility to study the subsurface in remote areas with minimum impact to environment (Polychronopoulou et al., 2020).

Passive seismic interferometry is cost-efficient methodology with relatively simple setup of field experiments. This methodology allows retrieving impulse response of a medium (Empirical Green's Function) from ambient seismic noise recorded at two receivers, assumed that the noise field is diffuse. If this condition is satisfied, it is possible to retrieve both surface and body waves from seismic noise by passive seismic interferometry based on either crosscorrelation, autocorrelation, deconvolution or cross-coherence of seismic records (Wapenaar et al., 2011). As shown in (Ricker and Claerbout, 1999) the condition of diffuse noise field is satisfied if the noise sources are distributed isotropically around seismic recorders and the noise registration time is long enough. The methodology to retrieve empirical Greens functions, using crosscorrelation or autocorrelation of ambient seismic noise, has been successfully applied in numerous studies (e.g. Shapiro and Campillo, 2004; Roux et al., 2005; Ruigrok et al., 2011; Draganov et al., 2009; Poli et al., 2012; Tibuleac et al., 2012; Wang et al., 2015; Taylor et al., 2016; Afonin et al., 2017; Oren and Nowack, 2016; Romero et al., 2018). In addition to ambient seismic noise interferometry, the coda wave interferometry was proposed (Campillo et al., 2003; Snieder et al., 2002; Snieder, 2006). This methodology is also widely used for different purposes, such as estimating nonlinear behavior in seismic velocity (Snieder et al., 2002), monitoring of stress changes inside the studied medium (Grêt et al., 2005, 2006) and determination of third order elastic constants in a complex solid (Payan et al., 2009). Numerous studies describe results of successful application of passive seismic interferometry for exploration and other applied geophysical purposes (e.g. Cheraghi et al., 2017; Roots et al., 2017; Dantas et al., 2018; Abraham et al., 2019; Polychronopoulou et al., 2020; Planès et al., 2020).

In spite of these numerous studies, there is the problem that the conditions of diffuse noise field from sources outside observation area (isotropic and homogeneous azimuthal distribution) of noise sources and long registration time) are difficult to satisfy in many practical situations. However, the diffuse wavefield for empirical Green's functions evaluation can exist also under other conditions. Wapenaar (2004) demonstrated that empirical Green functions could be retrieved from cross correlation of two recordings of a wavefield at different receiver locations at the free surface in the case when diffuse wavefield is produced by many uncorrelated sources inside the medium. Wapenaar and Thorbecke (2013) also considered conditions for empirical Green's function retrieval from ambient noise from a directional scatterer in a homogeneous embedding medium, illuminated by a directional noise field.



In our paper, we examine application of passive seismic interferometry for the case when noise is strongly directional and receiver array is semi-linear. For this, we use continuous seismic data recorded during XSoDEx (eXperiment of SODankylä Deep Exploration) project in northern Finland (Buske et al., 2019). We analyze the ambient seismic noise recorded by stations located in different sub-regions of the XSoDEx study area in order to understand spatial and temporal distribution of noise
70 sources. We perform numerical modelling of propagation of signals corresponding to identified noise sources through various synthetic models, representing certain types of heterogeneities (massive sulfides, mafic intrusions, faults). We show by numerical modelling that direct waves, generated by various sources are scattered on these heterogeneities and produce diffused wavefield. Therefore, empirical Greens function of the studied medium can be retrieved by crosscorrelation of this wavefield recorded at different locations (Wapenaar, 2004; Wapenaar and Thorbecke, 2013; van Manen et al., 2005). For
75 evaluation of empirical Greens functions, we apply advanced method of passive seismic interferometry (Afonin et al., 2019) that we called signal-to-noise ratio stacking (SNRS). We show results of application of passive seismic interferometry for mapping the uppermost crust in the area of XSoDEx project.

2 Experiment description

Within XSoDEx project, Geological Survey of Finland, TU Bergakademie Freiberg and University of Oulu acquired seismic reflection and refraction data using the Vibroseis truck of TU Bergakademie Freiberg during July and August 2017 resulting
80 in **four seismic profiles of total length of approximately 80 km**. The seismic refraction data were recorded by 60 vertical and 40 three-component Sercel Ltd. wireless autonomous **receivers** along an extended line around the reflection spread with maximum offsets of around 10 km. **During nighttime, the wireless receivers were recording passive seismic data**. Thus, the XSoDEx experiment provided a good opportunity to verify results of passive seismic interferometry with controlled-source
85 seismic data, to identify limitations of this technique in areas of generally low level of high-frequency anthropogenic noise and to propose possible improvements of known techniques.

The XSoDEx seismic survey was conducted in the Central Lapland Greenstone belt in Northern Finland, around Sodankylä region (Figure 1). Area is famous for its mineral deposits and active exploration, including operating Kittilä Gold mine west from the survey area and Kevitsa Ni-Cu mine that also has significant amounts of platinum, palladium, gold and cobalt. The
90 seismic survey lines are crossing varying geology including outcrops of Archean basement and layered mafic intrusions.

3 Ambient seismic noise in XSoDEx study area

In addition to microseismic noise, there are several local noise sources in the XSoDEx study area. They are industrial noise from Kevitsa Mine, traffic noise from the roads and water power plants of Kitinen River.

For estimation and comparison of noise level for different XSoDEx profiles, we used vertical components of ambient seismic noise recorded by wireless seismic stations. The wireless data was not acquired during nighttime on Sundays, when
95 anthropogenic activity is minimal. As one can see in Figure 2, the noise level and its frequency spectra differ significantly at stations located at different XSoDEx profiles.



The station V1 was installed in the area characterized by the highest noise level for all analyzed frequencies. It is likely caused by location of this station close to Kevitsa mine and dam. Seismic noise recorded by station P2 was characterized by lower level, than the seismic noise recorded by V1 station. Probably the main noise sources at that station were road and dam. A narrow peak at frequencies of about 26-30 Hz characterizes seismic noise at station V2. We suggest that the main noise source at the V2 was the dam. Unexpected results of noise level estimations were obtained for stations P2 and A. As one can see in Figure 2, station P2 is characterized by relatively high level of seismic noise. At the same time, seismic noise at point A is relatively low, despite similar distance from these stations to the dam and the road. We need to remember, however, that data acquisition along different profiles was made during different time periods, so probably one additional high-frequency noise source was acting at P2 during the data acquisition period.

It is clear that dominating noise sources are different in various areas of our study, and general condition for passive seismic interferometry (the sources need to be isotopically and homogeneously distributed around the study area) is not satisfied. However, local sources of high intensity can be used for evaluation of EGF for selected profiles. According to the result of spectral analysis and locations of potential noise sources, we proposed the next possible candidates for sources of signals for passive seismic interferometry.

- 1) Kevitsa mine, because all the profiles are located at distances of about 6 – 42 km from the mine;
- 2) Kitinen River, because three of four lines are located along river, and water power plants, because of three dams located along the river;
- 3) The waves that are scattered on heterogeneities as proposed by van Manen et. al. (2005), Wapenaar (2004), Wapenaar et. al. (2015).
- 4) We can also use the signals from vibrosource and blasts in XSoDEX experiment, in order to utilize propagation of surface waves to long offsets. Normally, in reflection experiment, only short offsets can be used and only shallow depth investigated. In the next chapter, we investigate the wavefield produced by these possible sources using numerical modelling.

4 Numerical modelling of seismic wavefield from different sources

For simulation of seismic wavefield propagation, we used SOFI3D software, which solves a wave equation by finite-difference method (<https://git.scc.kit.edu/GPIAG-Software/SOFI3D/tree/Release>). For simulation of scattered wavefield we developed synthetic model based on a-priori knowledge about geological structure of the study area (Leväniemi et al., 2018). We used background velocities of $V_p=5600$ m/s, $V_s=3500$ m/s and density= 2650 kg/m³ corresponding to felsic rocks. The embedded vertical high velocity bodies were representing mafic dykes of 30-150 m wide with depths varying randomly from 60 m to 600 m with the following physical properties (Figure 3): $V_p=6500$ m/s, $V_s=3700$ m/s, density 2800 kg/m³. We also assumed an uppermost 60 m thick layers representing quaternary sediments with $V_p=2000$ m/s, $V_s=1200$ m/s and density 1600 kg/m³. The following elastic properties of air were used as boundary conditions of the model: $V_p=330$ m/s, $V_s=0$, density =1.25 kg/m³. As sources, we used: 1) blast with dominant frequency of 30 Hz, 2) water power plant (stationary noise with frequency of 2.5 Hz), and plane waves with frequencies of 50 Hz and 2.5 Hz. In the modelling we used the grid size of 30 m.



The first synthetic signal was a plane wave originating from a source in the far-field area. The wave originated at the depth of 6000 m and arrived at the surface at **incidence angle of 45 degrees**. As one can see on synthetic seismogram in Figure 4, the recorded wavefield consists of the first arrival, several reflected waves and numerous scattered waves with apparent velocities of 2100-2500 m/s corresponding to surface waves. Figure 5 shows an example of particle motion diagrams (Figure 5, c) and results of spectral analysis of these arrivals (Figure 5, b). Due to elliptical polarization and dependence of phase velocity on frequency, one can conclude, that these waves are surface Rayleigh waves. As these surface waves have stochastic directivities, superposition of them may be considered as diffused wavefield that can be used, in principle, to estimate Empirical Greens functions.

In this synthetic example, we demonstrate that the diffuse wavefield consisting of low-frequency surface waves (Rayleigh) can be produced by scattering of a plane wave at velocity heterogeneities. We considered monochromatic plane wave, but in real in ambient noise, many frequencies present and scattering would be more pronounced.

The second example simulate propagation of the signal originating from production blast in Kevitsa mine. Figure 6 shows results of **modelling of the wavefield produced by the blast** and propagating in the model with stochastically distributed heterogeneities. As seen, the wavefield consists of only direct P-wave arrival, reflected P-wave, multiples of P-waves, reflected from vertical heterogeneities, and surface Love wave. **In that case, surface Rayleigh waves are absent from the wavefield.**

The third synthetic example corresponds to the direct wave continuously produced by waterpower plant, which could also be scattered on heterogeneities and produce diffused wavefield. As an input signal for simulation, we used a real seismogram recorded by station V1, which was located at the shortest distance from the waterpower plant (Figure 2). The spectral-time diagram of the signal is presented in Figure 7. As one can see, there are several spectral peaks with frequencies of about 5 Hz, 12.5 Hz and 20-50 Hz. According to (Antonovskaya et al., 2017; 2019), seismic noise generated by waterpower plants may correspond to a set of spectral peaks between 3.6 Hz and about 50 Hz. Other spectral peaks could be due to production activities (transportation, excavation etc.) at Kevitsa mine. Therefore, in this case we have complex contribution of all sources to the noise wavefield.

Figure 8 (a) shows synthetic seismograms of stationary wavefield produced by the signal, spectrogram of which is presented in Figure 7. Analysis of particle motion (Figure 8 (c)) shows that this stationary field is consisting of Rayleigh waves with apparent velocities of about 2100-2500 m/s. Figure 8(b) shows crosscorrelations of the first trace with all other traces in Fig. 8(a). As seen, the wavefield contains also P and S waves.

Results of our synthetic modeling demonstrate that the plane wave scattered at heterogeneities satisfies condition of diffuse wavefield and hence can be used to extract EGFs. The stationary signal from the power plant can also be used in the cases when receivers are deployed within the first Fresnel volume area. Usage of the diffuse wavefield produced by scattering on local heterogeneities or stationary wavefield from a single source will have an advantage that in both cases the long registration time necessary for obtaining isotropic azimuthal coverage of ambient noise sources is not required. However, special analysis of the continuous data would be necessary, in order to extract the diffuse wavefield from the data. For this purpose, **the SNRS algorithm described earlier in Afonin et al. (2019) can be used.**



165 4 Verifying passive seismic interferometry with diffuse wavefield with passive seismic data recorded during XSoDEx experiment

In order to demonstrate application of passive seismic interferometry with the scattered diffuse wavefield, we used passive seismic data acquired in the XSoDEx experiment and applied the SNRS algorithm of EGFs evaluation. From the XSoDEx lines, one is particularly suitable for such demonstration. In this short high-resolution profile (green line in Fig. 9) of total length of 1000 m both 1C and 3C Sercel wireless units were installed at distances of 10 m. The 3C sensors were installed between 1C sensors at distances varying from 20 to 30 m. The results of passive seismic interferometry along this line can be also verified using the active source seismic data acquired along the same line and results of previous geophysical experiments and drilling in this area.

For dispersion curve calculation, we used continuous passive seismic data recorded during the period of 21.08.2017 – 23.08.2017. We made no any a-priori assumptions about the nature and spatial distribution of noise sources. For calculation of EGFs, we applied such pre-processing procedures as removing mean and trend, spectral whitening and pre filtering by the band pass filter of 1-100 Hz. After this, we calculated crosscorrelation functions so that virtual sources of impulse signal were placed in the beginning, in the middle and in the end of the profile. The choice of virtual source positions is based on the wavelength of the analyzed signal, which is about 400m. An example of EGFs calculated with the SNRS algorithm and the correspondent dispersion curve are presented in Figure 10.

As seen from particle motion diagram calculated for one of the 3C sensors, the main arrival seen in EGFs corresponds to Rayleigh wave. A good correlation of waveforms of dispersed surface wave is also seen.

For calculation of velocity models from dispersion curves, we used Geopsy software (www.geopsy.org). We applied global optimization algorithm with 500 iterations to obtain the best solution. The starting model consisted of three major layers with properties presented in Table 1. The range of each property was selected using information about physical properties of rocks in the study area available from literature (Schön, 2015).

Table 1 – Starting model of the medium, used for inversion of dispersion curves.

Depth	V _p , m/s	V _s , m/s	Rho, kg/m ³	rock types
1-50	700-1200	350-900	1200-1500	quaternary deposits, coarse-grained sorted sediments
50-200	5900-6200	1800-3600	2000-2300	granite, felsic volcanic rocks
200-500	6300-6600	3300-3600	2000-2500	mafic volcanic rocks

190 We calculated 1D velocity models for receivers at each 100 m of the profile and obtained a 2D model presented on Figure 11(a). The subplots 11(b) and 11(c) present results of global optimization of one selected dispersion curve. One interesting feature of this model is a layer with S-wave velocities of about 200-400 m/s and thickness of 20-38 m that may correspond to



195 thick sediments. The thickness of sediments agrees well with the result of Åberg et al. (2017), who used GPR measurements and drilling information to obtain sedimentary thickness in this area. The velocities of S-waves beneath sedimentary cover will be discussed in Section 5.

We applied the same technique of EGFs calculation to the data with lower spatial resolution recorded along the part of Sakatti profile shown by blue in Figure 9. Particle motion diagram (Figure 12(c)) shows that evaluated EGFs contain mainly surface waves. Dispersion curves were calculated for each 500 m of the profile for obtaining 2D velocity model. For this, the virtual sources were placed at each 500 m and all neighbour receivers, located at distances no longer than 1000 m from the virtual source receivers. For calculation of dispersion curves, MASW technique was used.

200 As one can see in Figure 12, advanced method of passive seismic interferometry allowed to us evaluate dispersion curve for frequencies of about 3-7 Hz. Inversion of dispersion curves was used to obtain 1D velocity models that were combined into 2D model (Figure 13(a)).

For verification of the modelling results we compared the velocity model in Figure 13(a) with the model obtained by inversion of dispersion curves estimated from surface waves produced by controlled source for the same part of Sakatti line (Figure 13 (b)). As seen, the velocity models reveal the same details and the velocities are generally in good agreement. The differences in velocities are of the order of 100 m/s in the central part of the profile. The largest difference up to 600 m/s can be seen in the beginning of the profile (from 15000 to 15500 m) and it can be explained either by uncertainty in dispersion curves extraction or by inversion errors.

210 **5 Shear-wave velocity models obtained using vibrotrack signal scattered at heterogeneities**

Surface waves recorded in active source experiments (ground roll) usually considered as non-wanted signal and removed from the data during processing. However, S-wave velocity models can be obtained from Vibroseis© surface waves using MASW method (Al-Husseini et al., 1981; Mari, 1984; Gabriels et al., 1987; Park et al., 1999). In this case, the depth resolution for S-wave velocity models is limited to several meters due to short offsets and small registration time in near-vertical reflection data. As the data in XSoDEx experiment was recorded at long offsets with the wireless equipment, such recordings can be used to obtain the S-wave velocities at larger depths.

220 Examples of raw shot gathers of Vibroseis© signals recorded in reflection experiment are presented in Buske et al. (2019). They used bandpass filters of 30-40-100-120 Hz to eliminate surface waves from raw reflection data. Vibrator sweep frequencies were from 10 to 170 Hz. In raw reflection data the surface waves arrivals can be followed up to 2-3 sec to rather short offsets of about 350 - 400 m. An example of record section compiled from wireless recorders data is presented in Figure 14. In this section a vibrator signal, presented in Figure 15, was correlated with the traces recorded at long offsets. The distance between traces in Figure 14 is 160 m. In Figure 14 one can see the first arrival of P-wave with velocity of about 5400 m/s and direct Rayleigh wave with velocity of about 880 m/s in frequency band of 20–100 Hz (Figure 14 (b)) that can be followed to offsets of about 1 km. In the frequency band of 1-10 Hz (Figure 14 (a)), surface waves cannot be followed to long offsets. The



225 surface wave arrivals that can be correlated appear on several traces close to shot. As seen in Figure 15 (b), the frequencies of
the vibrator signal start from about 12 Hz and no lower frequencies are present.

**We used the SNRS technique and continuous seismic recordings of XSoDEx experiment to obtain EGFs for all the XSoDEx
profiles.** In all EGFs the main phase seen was Rayleigh wave (Figure 16). The EGFs were used to obtain dispersion curves
and invert them using Geopsy inversion software and model parameters, presented in Table 1. The 2D velocity models to the
230 depth of 300 m for all XSoDEx profiles obtained by interpolation of 1D velocity models are presented in Figure 17, in which
also the **boundaries of major lithological units** from Figure 1 are indicated. All the velocity models are shown in the same color
scale. The S-wave velocities along the XSoDEx are generally varying from very low values of 200-400 m/s detected in some
places to 3200 m/s. The uppermost layer with velocities of 200-400 m/s and thickness up to 50 m corresponds to quaternary
sediments, and the boundary between this layer and the lowermost part of velocity models is indicated also by velocity contrast
235 in 1D models. Independent information about thickness of sediments in our study area obtained by direct drilling shows that
the thickness of quaternary sediments there is limited to several dozens meters. That is why it can be concluded that S-wave
velocities in the range of 800-3200 m/s correspond to different types of basement rocks. As these values are generally much
lower than the values of S-wave velocities for the rocks of Fennoscandian Shield obtained by laboratory measurements on
rock samples (Kern et al., 1993, Dortman, 1992), they cannot be interpreted directly in terms of rock composition.

240 One possible explanation is that the low values of shear wave velocities might be caused by non-zero azimuths to noise sources.
However, it was demonstrated by previous studies that non-zero azimuth increases apparent velocity (e.g. Sadeghisorkhani et
al., 2016). That is why it is necessary to find another explanation of generally low S-wave velocities of the basement rock in
our study.

The S-wave velocities in the uppermost crust down to several kilometers were previously evaluated using surface waves by
245 Pedersen and Campillo (1991), Grad and Luosto (1992), Grad et al. (1998). They reveal low values of S-wave velocity in the
shallow crust and low values of quality factor that is rapidly increasing at the depth of about 1 km. Moreover, Grad et al. (1998)
found that the quality factor in the Archean shallow crust of the Fennoscandian Shield is lower than that in the Proterozoic
crust. Grad and Luosto (1992) explained the low quality factor in the uppermost 1 km of the crust by increased cracks density.
Therefore, increased crack density can explain also generally low S-wave velocities of the basement rocks revealed by our
250 study. Consider that the wave is propagating through fractured medium consisting of granites and the fractures are filled with
some clastic rocks. If the S-wave velocities in the granitic rock are about 3300 m/s and those in the clastic rocks are about 400
m/s (similar to the velocity in quaternary deposits), then the averaged velocity would be about 1700-2000 m/s, depending on
crack density. Taking the general effect of fracturing into account, we conclude that the values of S-wave velocities lower
than 2000 m/s correspond to felsic rock, while the higher values of velocity correspond to mafic and ultramafic rocks (Figure
255 17).



6 Conclusions

In our study, we used recordings of ambient noise recorded during short time period in a generally quiet area with low level of anthropogenic noise. We showed that the noise was non-stationary and the azimuthal distribution of noise sources was neither isotropic nor heterogeneous during the data acquisition period. In spite of that, we obtained good quality EGFs and dispersion curves and the S-wave velocity models showing presence and thickness of quaternary sedimentary cover and velocity heterogeneities in the bedrock that agree well with the geological data. We explain this by the fact that the ambient noise recorded during the XSoDEx experiment contained a large proportion of diffused wavefield produced by scattering of plane waves from distant sources and ballistic waves produced by certain types of non-stationary sources on stochastically distributed heterogeneities in the uppermost crust. We demonstrated by numerical modelling that certain types of geological structures, particularly those composed of rocks with contrasting elastic properties, could scatter plane waves and ballistic waves from non-stationary sources and produce scattered Rayleigh waves. This scattered wavefield together with the ballistic wavefield from non-stationary sources can be used for EGFs evaluation, if the special algorithm of signal-to-noise ratio stacking (SNRS) is applied. Our result is a practical illustration of the conclusions about retrieval of EGF from the scattered wavefield revealed previously by Wapenaar (2004) and Wapenaar and Thorbecke (2013). In certain geological areas, extraction of EGFs from the wavefield scattered at heterogeneities provides an opportunity to reduce the time for short-term passive seismic experiments.

7 Acknowledgements

The XSoDEx project was realised as a joint effort of Geological Survey of Finland (coordinator), TU Bergakademie Freiberg, Institute of Geophysics and Geoinformatics, Freiberg, Germany, and University of Oulu. The wireless equipment of the University of Oulu is jointly operated by Oulu Mining School and Sodankylä Geophysical Observatory of the University of Oulu. The field work of the University of Oulu personnel in summer, 2017 was supported by the Renlund Foundation. Financial support for processing and interpretation of the XSoDEx data used in this study was provided by Geological Survey of Finland in 2018. Thanks to Sodankylä Geophysical Observatory staff for their kind assistance during XSoDEx survey. Particular thanks are to Hanna Silvennoinen, Jouni Nevalainen, Kari Moisio, Jari Karjalainen and Tommi Pirttisalo, whose participation in XSoDEx field survey was particularly important for safe and reliable operation of Sercel Ltd wireless equipment. Many thanks to Henrik Jänkäväära for his contribution in XSoDEx data processing.

The authors wish to acknowledge CSC – IT Center for Science, Finland, for computational resources. The numerical modelling of wavefields, presented in the work was funded by the Russian Ministry of Education and Science by a research project of state assignment ‘Development of seismic methods for forecasting and reducing the consequences of natural and man-made disasters in the Western Arctic sector of the Russian’ (0409-2015-0135, №AAAA-A18-118012490072-7).



References

- Åberg, A. K., Salonen, V. P., Korkka-Niemi, K., Rautio, A., Koivisto, E., Åberg, S. C.: GIS-based 3D sedimentary model for visualizing complex glacial deposition in Kersilö, Finnish Lapland, *Boreal environment research*, 22, 277-298, <http://hdl.handle.net/10138/257516>, 2017
- 290 Abraham, E. M., Alile, O. M.: Modelling subsurface geologic structures at the Ikogosi geothermal field, southwestern Nigeria, using gravity, magnetics and seismic interferometry techniques, *Journal of Geophysics and Engineering*, 16(4), 729-741, <https://doi.org/10.1093/jge/gxz034>, 2019
- Afonin, N., Kozlovskaya, E., Kukkonen, I., and DAFNE/FINLAND Working Group: Structure of the Suasselkä postglacial fault in northern Finland obtained by analysis of local events and ambient seismic noise, *Solid Earth*, 8, 531-544, <https://doi.org/10.5194/se-8-531-2017>, 2017.
- 295 Afonin, N., Kozlovskaya, E., Nevalainen, J., Narkilahti, J.: Improving the quality of empirical Green's functions, obtained by cross-correlation of high-frequency ambient seismic noise, *Solid Earth*, 10(5), 1621-1634, <https://doi.org/10.5194/se-10-1621-2019>, 2019
- Al-Husseini, M. I., Glover, J. B., Barley, B. J.: Dispersion patterns of the ground roll in eastern Saudi Arabia, *Geophysics*, 300 46.2, 121-137, <https://doi.org/10.1190/1.1441183>, 1981
- Antonovskaya, G.N., Kapustian, N.K., Moshkunov, A.I., Danilov, A.V., Moshkunov, K.A.: New seismic array solution for earthquake observations and hydropower plant health monitoring, *Journal of Seismology*, 21, 1039-1053, <https://doi.org/10.1007/s10950-017-9650-8>, 2017
- Antonovskaya, G., Kapustian, N., Basakina, I., Afonin, N., Moshkunov, K.: Hydropower Dam State and Its Foundation Soil Survey Using Industrial Seismic Oscillations, *Geosciences*, 9(4), 187, <https://doi.org/10.3390/geosciences9040187>, 2019
- 305 Buske, S., Hlousek, F., Jusri, T., XSoDEX: Reflection seismic data acquisition and processing report, Institute of Geophysics and Geoinformatics TU Bergakademie Freiberg, Germany, 57 pp., 2019
- Campillo, M., and Paul, A.: Long-range correlations in the diffuse seismic coda, *Science*, 299(5606), 547-549, DOI: 10.1126/science.1078551, 2003
- 310 Cheraghi, S., White, D. J., Draganov, D., Bellefleur, G., Craven, J. A., Roberts, B.: Passive seismic reflection interferometry: A case study from the Aquistore CO₂ storage site, Saskatchewan, Canada, *Geophysics*, 82(3), B79-B93, <https://doi.org/10.1190/geo2016-0370.1>, 2017
- Dantas, O. A. B., do Nascimento, A. F., Schimmel, M.: Retrieval of body-wave reflections using ambient noise interferometry using a small-scale experiment, *Pure and Applied Geophysics*, 175(6), 2009-2022, <https://doi.org/10.1007/s00024-018-1794-0>, 2018
- 315 Dortman, N. B.: *Handbook Petrophysics*, Nedra, Moscow, 390 pp, 1992
- Draganov, D., Campman, X., Thorbecke, J., Verdel, A., Wapenaar, K.: Reflection images from ambient seismic noise, *Geophysics*, 74(5), 63-67, <https://doi.org/10.1190/1.3193529>, 2009



- Gabriels, P., Snieder, R., Nolet, G.: In situ measurements of shear-wave velocity in sediments with higher-mode Rayleigh waves, *Geophysical prospecting*, 35.2, <https://doi.org/10.1111/j.1365-2478.1987.tb00812.x>, 187-196, 1987
- 320 Grad, M., and Luosto, U.: Fracturing of the crystalline uppermost crust beneath the SVEKA profile in Central Finland, *Geophysica*, 28.1-2, 53, 1992
- Grad, M., Czuba, W., Luosto, U., Zuchniak, M.: QR factors in the crystalline uppermost crust in Finland from Rayleigh surface waves, *Geophysica*, 34(3), 115-129, 1998
- 325 Grêt, A., Snieder, R., Aster, R. C., Kyle, P. R.: Monitoring rapid temporal change in a volcano with coda wave interferometry, *Geophysical Research Letters*, 32(6), <https://doi.org/10.1029/2004GL021143>, 2005
- Grêt, A., Snieder, R., Scales, J.: Time-lapse monitoring of rock properties with coda wave interferometry, *Journal of Geophysical Research: Solid Earth*, 111(B3), <https://doi.org/10.1029/2004JB003354>, 2006
- Kern, H., Walther, C., Flüh, E. R., Marker, M.: Seismic properties of rocks exposed in the POLAR profile region—constraints on the interpretation of the refraction data, *Precambrian Research*, 64 (1-4), 169-187, [https://doi.org/10.1016/0301-9268\(93\)90074-C](https://doi.org/10.1016/0301-9268(93)90074-C), 1993
- 330 Leväniemi, H., Melamies, M., Mertanen, S., Heinonen, S., Karinen, T.: Petrophysical measurements to support interpretation of geophysical data in Sodankylä, northern Finland, *Geological Survey of Finland Open File Work Report 25/2018*, 2018
- Mari, J. L.: Estimation of static corrections for shear-wave profiling using the dispersion properties of Love waves, *Geophysics*, 335 49(8), 1169-1179, <https://doi.org/10.1190/1.1441746>, 1984
- Oren, C. and Nowack, R. L., Seismic body-wave interferometry using noise auto-correlations for crustal structure, *Geophysical Journal International*, 208(1), 321-332, <https://doi.org/10.1093/gji/ggw394>, 2016
- Park, C. B., Miller, R. D., Xia, J.: Multichannel analysis of surface waves, *Geophysics*, 64(3), 800-808, <https://doi.org/10.1190/1.1444590>, 1999
- 340 Payan, C., Garnier, V., Moysan, J., Johnson, P. A.: Determination of third order elastic constants in a complex solid applying coda wave interferometry, *Applied Physics Letters*, 94(1), 011904, <https://doi.org/10.1063/1.3064129>, 2009
- Pedersen, H., and Campillo, M.: Depth dependence of Q beneath the Baltic Shield inferred from modeling of short period seismograms, *Geophysical research letters*, 18.9, 1755-1758, <https://doi.org/10.1029/91GL01693>, 1991
- 345 Planès, T., Obermann, A., Antunes, V., Lupi, M.: Ambient-noise tomography of the Greater Geneva Basin in a geothermal exploration context, *Geophysical Journal International*, 220(1), 370-383, <https://doi.org/10.1093/gji/ggz457>, 2020
- Poli, P., Pedersen, H. A., Campillo, M., POLENET/LAPNET Working Group.: Emergence of body waves from cross-correlation of short-period seismic noise, *Geophysical Journal International*, 188(2), 549-558, <https://doi.org/10.1111/j.1365-246X.2011.05271.x>, 2012
- Polychronopoulou, K., Lois, A., Draganov, D.: Body-wave passive seismic interferometry revisited: mining exploration using the body waves of local microearthquakes, *Geophysical Prospecting* 68.1-Cost-Effective and Innovative Mineral Exploration Solutions, 232-253, <https://doi.org/10.1111/1365-2478.12884>, 2020
- 350 Reid, K. J.: The Importance of Minerals and Mining, Online Lecture, University of Minnesota, 2011



- Rickett, J. and Claerbout, J.: Acoustic daylight imaging via spectral factorization: helioseismology and reservoir monitoring, *Geophysics*, 18, 957-960, <http://dx.doi.org/10.1190/1.1438420>, 1999
- 355 Romero, P. and Schimmel, M.: Mapping the basement of the Ebro Basin in Spain with seismic ambient noise autocorrelations, *Journal of Geophysical Research: Solid Earth*, 123(6), 5052-5067, <https://doi.org/10.1029/2018JB015498>, 2018
- Roots, E., Calvert, A. J., Craven, J.: Interferometric seismic imaging around the active Lalor mine in the Flin Flon greenstone belt, Canada, *Tectonophysics*, 718, 92-104, <https://doi.org/10.1016/j.tecto.2017.04.024>, 2017
- Roux, P., Sabra, K.G., Gerstoft, P., Kuperman, W.A., Fehler, M.C.: P-waves from cross-correlation of seismic noise, *Geophysical Research Letters*, 32, L19303, doi:10.1029/2005GL023803, 2005
- 360 Ruigrok, E., Campman, X., Wapenaar, K.: Extraction of P-wave reflections from microseisms, *Comptes Rendus Geoscience*, 348(8-9), 512-525, <https://doi.org/10.1016/j.crte.2011.02.006>, 2011
- Sadeghisorkhani, H., Gudmundsson, Ó., Roberts, R., Tryggvason, A.: Mapping the source distribution of microseisms using noise covariogram envelopes, *Geophysical Journal International*, 205(3), 1473-1491, <https://doi.org/10.1093/gji/ggw092>, 2016
- 365 Shapiro, N. and Campillo, M.: Emergence of broadband Rayleigh waves from correlations of the ambient seismic noise, *Geophysical Research Letters*, 31.7, <https://doi.org/10.1029/2004GL019491>, 2004
- Schön, J.H.: *Fundamentals and principles of petrophysics*, 2nd edition. Elsevier, 512 pp, 2015
- Snieder, R., Grêt, A., Douma, H., Scales, J.: Coda wave interferometry for estimating nonlinear behavior in seismic velocity, *Science*, 295(5563), 2253-2255, DOI: 10.1126/science.1070015, 2002
- 370 Snieder, R.: The theory of coda wave interferometry, *Pure and Applied geophysics*, 163(2-3), 455-473, <https://doi.org/10.1007/s00024-005-0026-6>, 2006
- Taylor, G., Rost, S., Houseman, G.: Crustal imaging across the North Anatolian Fault Zone from the autocorrelation of ambient seismic noise, *Geophysical Research Letters*, 43, 2502–2509, <https://doi.org/10.1002/2016GL067715>, 2016
- Tibuleac, I. M. and von Seggern, D.: Crust–mantle boundary reflectors in Nevada from ambient seismic noise autocorrelations, *Geophysical Journal International*, 189(1), 493–500, <https://doi.org/10.1111/j.1365-246X.2011.05336.x>, 2012
- 375 van Manen, D. J., Curtis, A., Robertsson, J. O.: Interferometric modeling of wave propagation in inhomogeneous elastic media using time reversal and reciprocity, *Geophysics*, 71(4), SI47-SI60, <https://doi.org/10.1190/1.2213218>, 2006
- Vasara, H.: State and outlook of the mining industry, MEAE Business Sector Services, Spring 2018, Sector Reports, Ministry of Economic Affairs and Employment of Finland, <http://urn.fi/URN:ISBN:978-952-327-297-2>, 2018
- 380 Wang, T., Song, X., Han, H. X.: Equatorial anisotropy in the inner part of Earth's inner core from autocorrelation of earthquake coda, *Nature Geoscience*, 8, 224-227, <https://doi.org/10.1038/ngeo2354>, 2015
- Wapenaar, K.: Retrieving the Elastodynamic Green's Function of an Arbitrary Inhomogeneous Medium by Cross Correlation, *Physical review letters*, 93(25), 254301, <https://link.aps.org/doi/10.1103/PhysRevLett.93.254301>, 2004



385 Wapenaar, K., Van Der Neut, J., Ruigrok, E., Draganov, D., Hunziker, J., Slob, E., Snieder, R.: Seismic interferometry by crosscorrelation and by multidimensional deconvolution: A systematic comparison, *Geophysical Journal International*, 185(3), 1335-1364, <https://doi.org/10.1111/j.1365-246X.2011.05007.x>, 2011

Wapenaar, K. and Thorbecke, J.: On the retrieval of the directional scattering matrix from directional noise, *SIAM Journal on Imaging Sciences*, 6(1), 322-340, <https://doi.org/10.1137/12086131X>, 2013

390

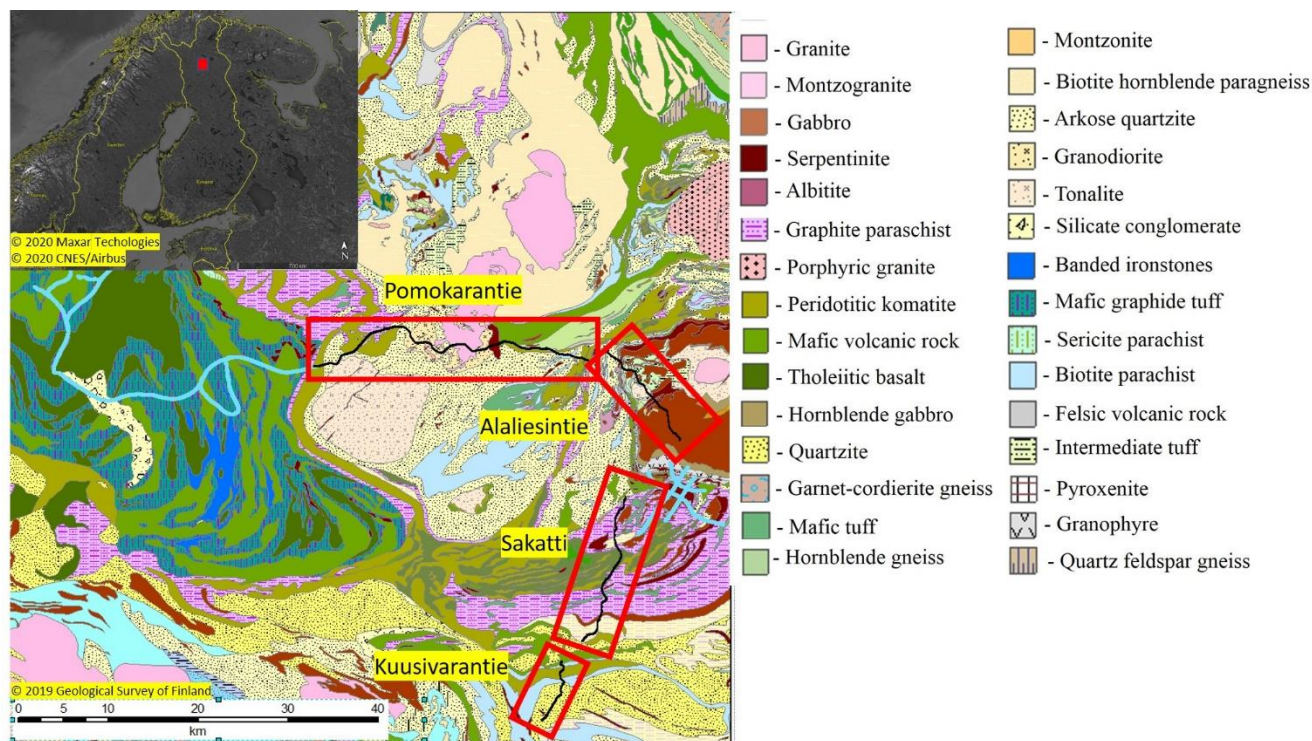
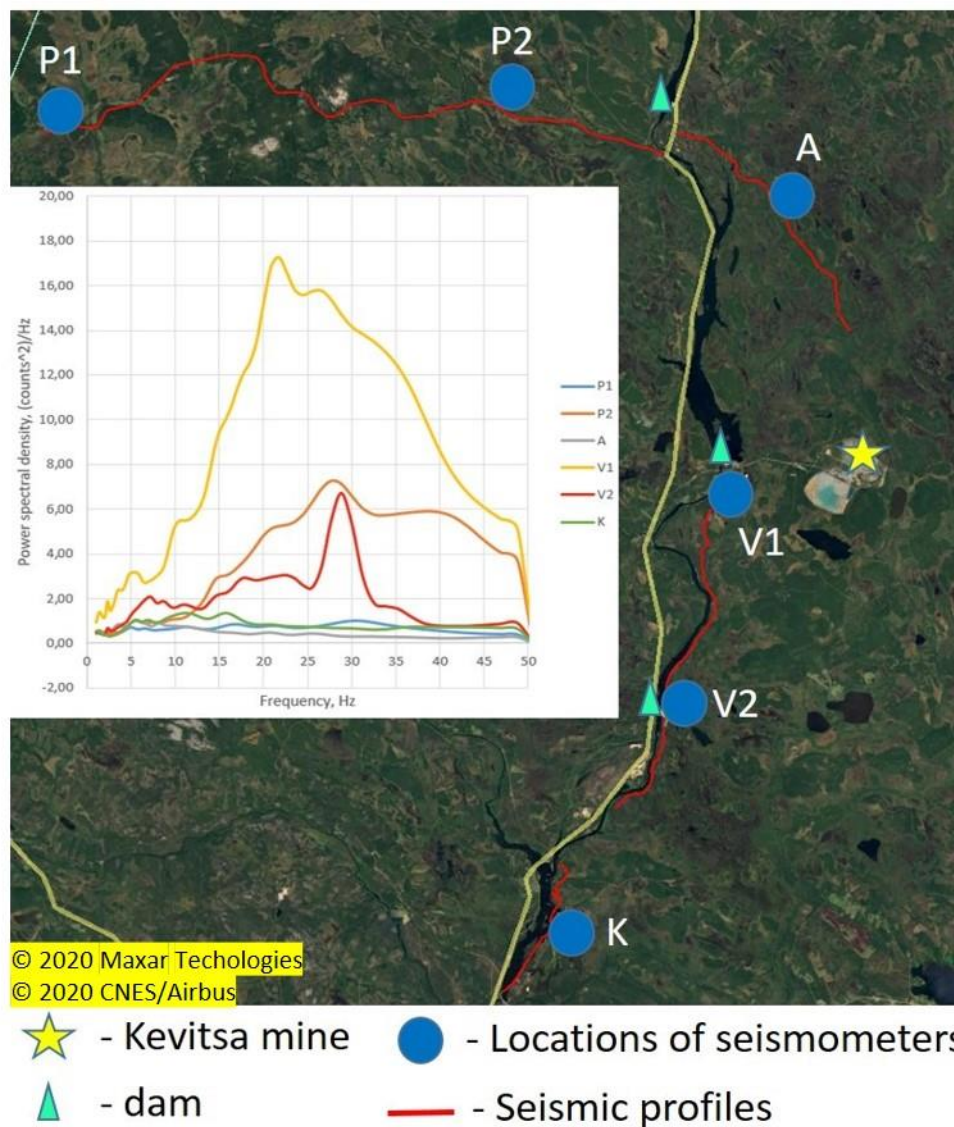
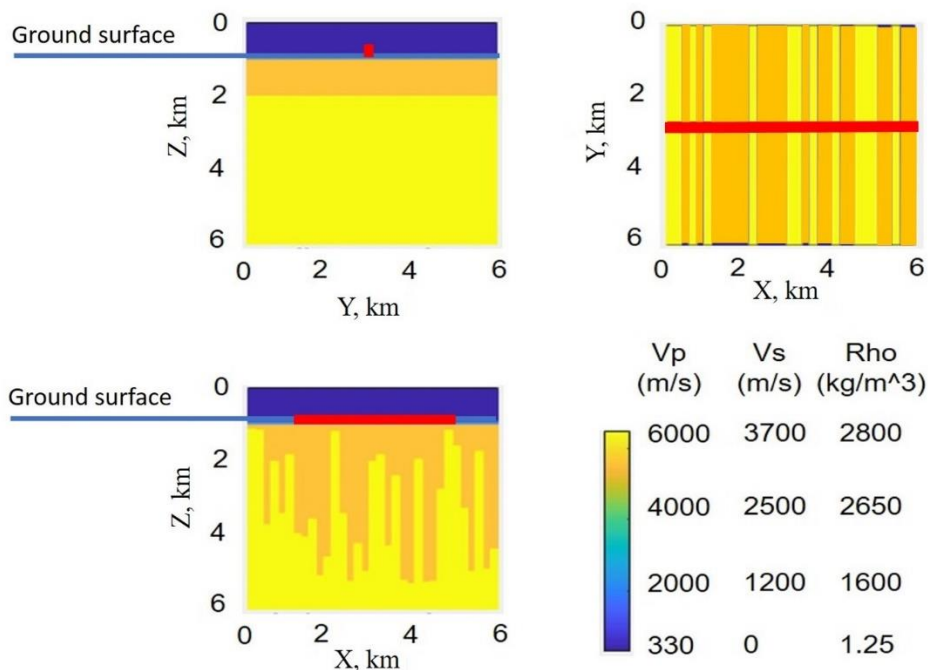


Figure 1: Geological map of XSoDEx study area (Buske et. al., 2019). The XSoDEx survey lines are shown with black lines. Previous seismic reflection survey lines are plotted with blue lines.



395 **Figure 2: Illustration of noise level at four stations located in different profiles of XSoDEx experiment. Position of strong noise sources (Kevitsa mine and dams of water power stations) and seismic stations selected for analysis are indicated. Yellow lines show roads. Inset figure shows comparison of ambient noise power spectral density estimated at selected stations.**



400 **Figure 3: The synthetic model used for investigation of wave propagation. Position of the seismic profile marked by the red line. Low velocity corresponding to the air is indicated on the top by blue colour.**

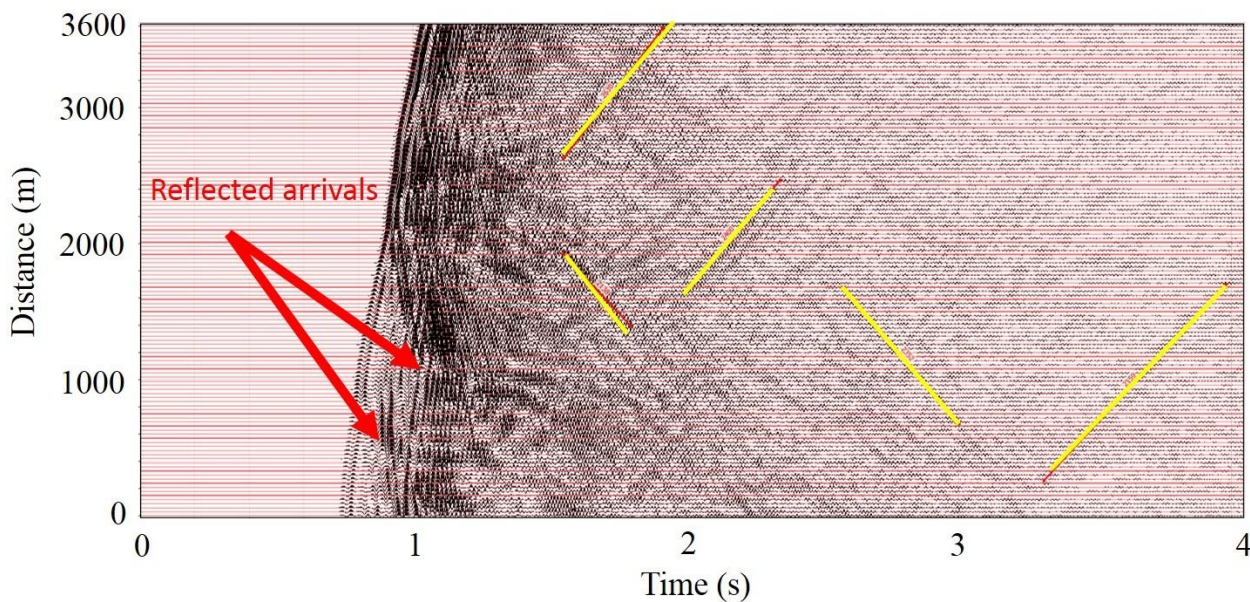
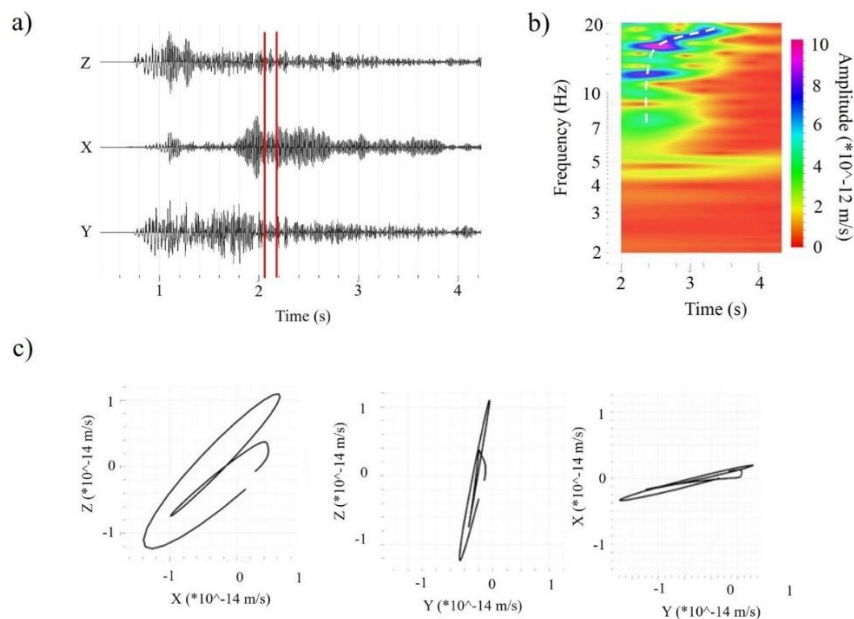
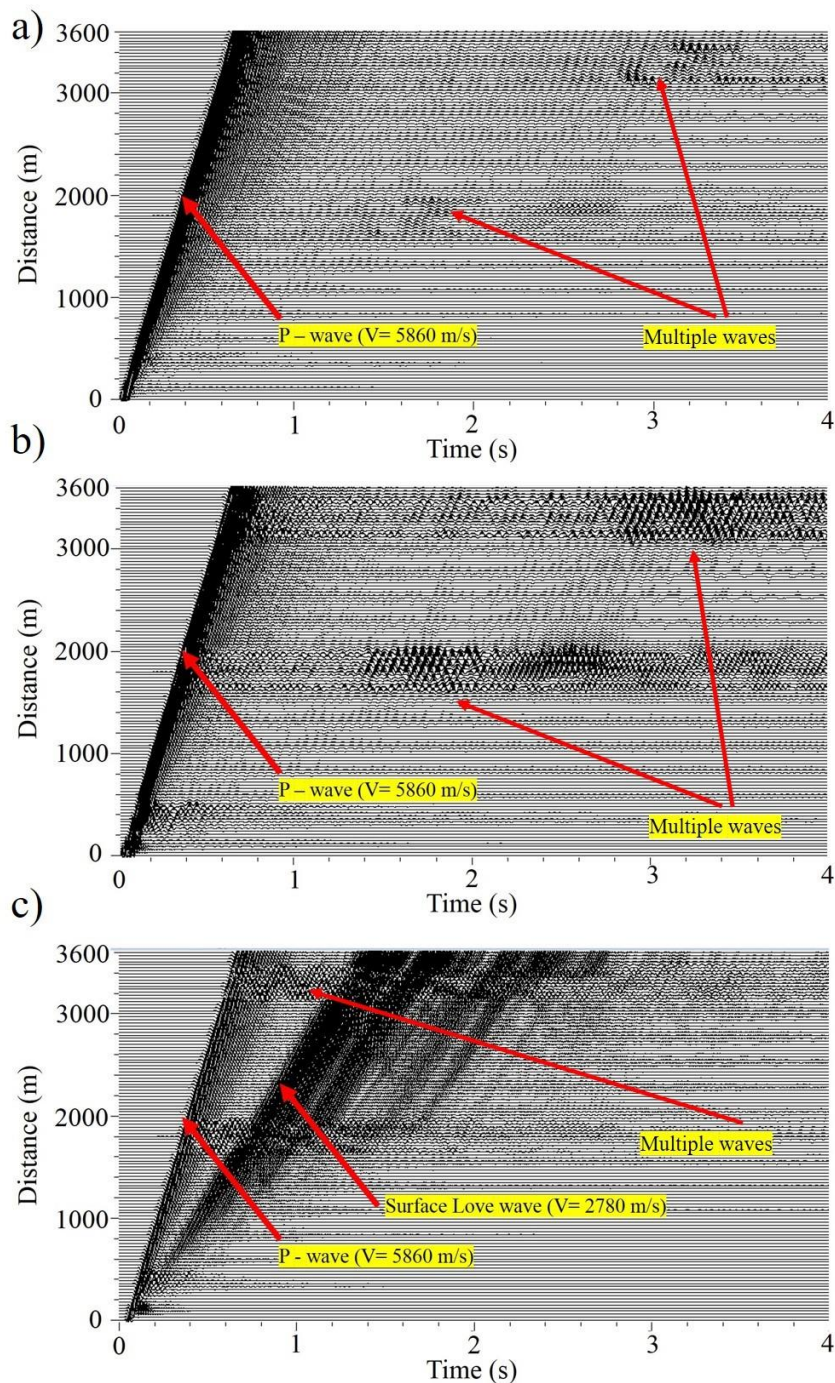


Figure 4: Synthetic seismogram (vertical component) of plane wave propagation through the synthetic model (0-4 sec), first arrival and reflections. From about 1.5 seconds we can see scattered arrivals with apparent velocity of 2100 -2500 m/s. Several arrivals of scattered waves are marked by yellow lines.



405

Figure 5: Result of analysis of scattered arrivals in synthetic seismograms with apparent velocity of 2100 -2500 m/s for frequencies 2-20 Hz in Fig. 4: a) 3C seismogram, recorded at distance of 2000 m in the seismogram shown in Figure 4; b) spectrogram of the vertical component (white dashed line corresponds to dispersion curve, picked by amplitude maximums); c) particle motion diagrams, calculated using part of seismogram indicated by red lines in Figure 5 (a), which corresponds to scattered wavefield.



410

Figure 6: Synthetic seismograms of the blast: a) vertical channel Z; b) horizontal channel X; c) horizontal channel Y.

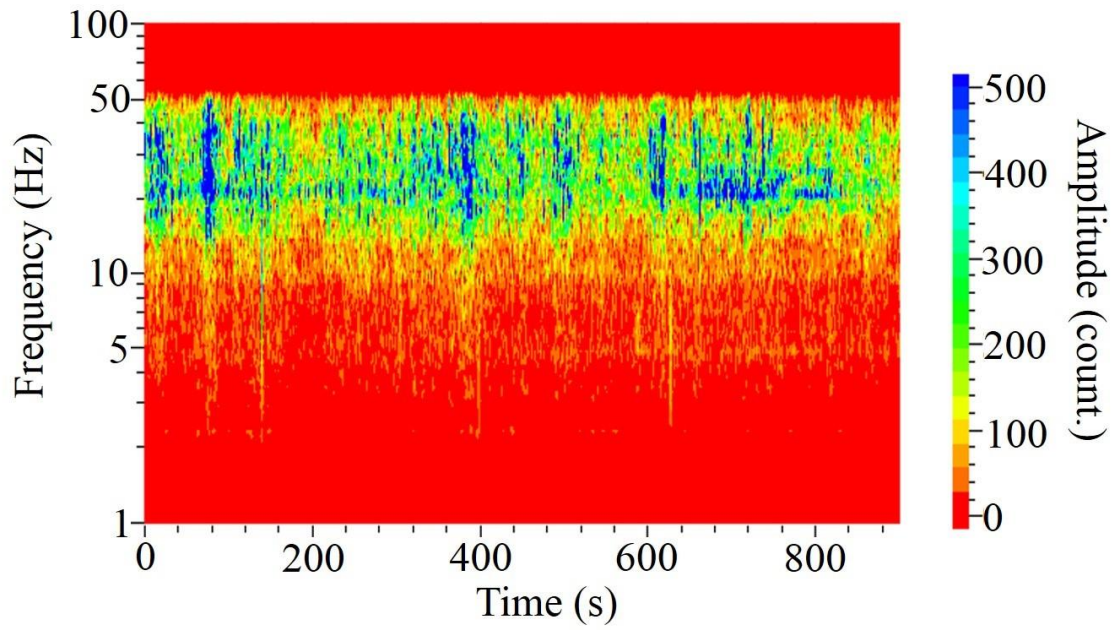
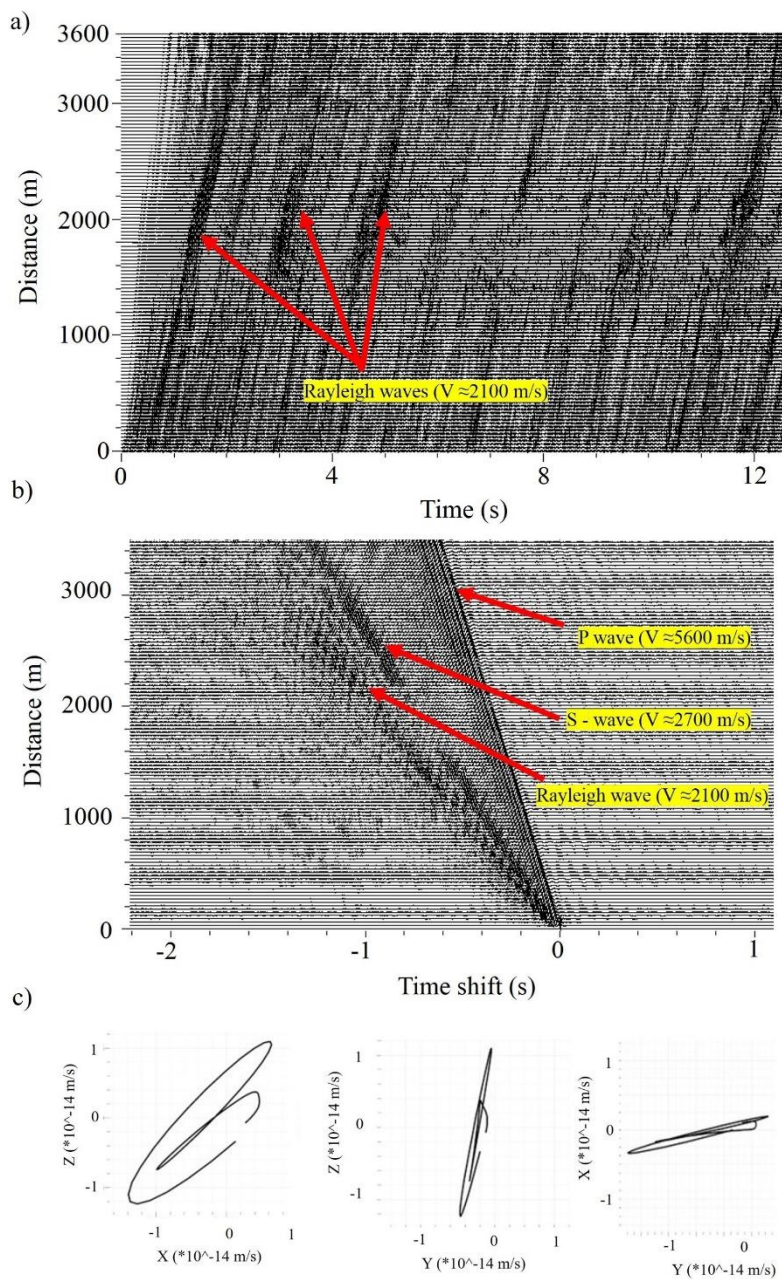
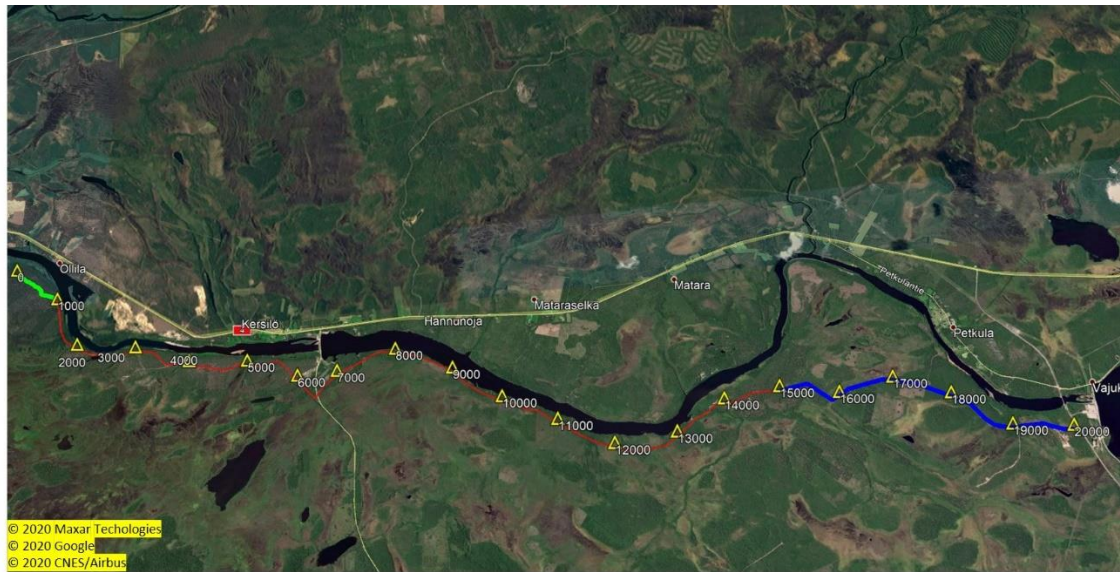


Figure 7: Spectrogram of the signal recorded by station V1 (Figure 2) and used as a wavefield of the source in simulation.



415 **Figure 8:** Synthetic seismograms of the signal with the spectrogram presented in Fig. 7 and propagating in synthetic model shown in Fig. 3: a) seismograms of vertical components; b) crosscorrelation functions of vertical components, calculated between the first and all other traces; c) particle motion diagram of Rayleigh wave.



420 **Figure 9: Location of passive seismic profiles of XSoDEx Sakatti line: green line – high-resolution profile; blue line – profile of lower-resolution.**

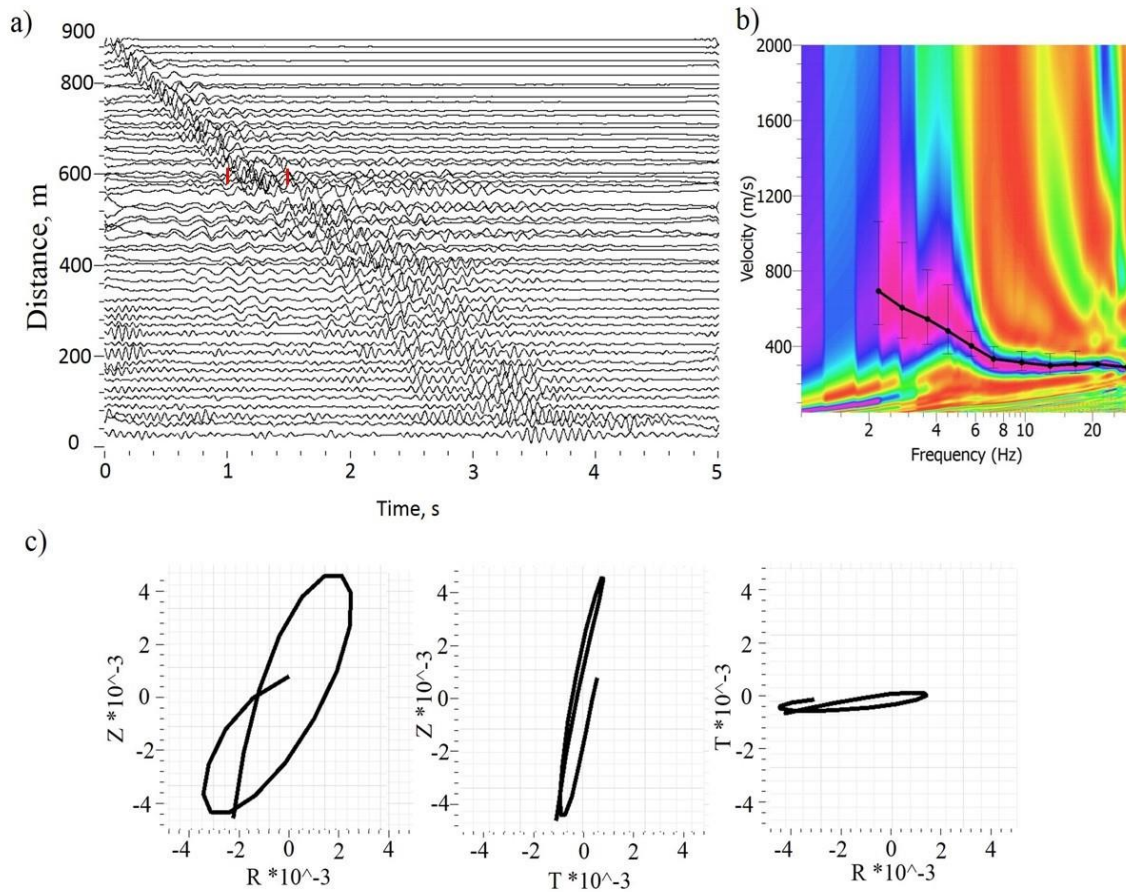
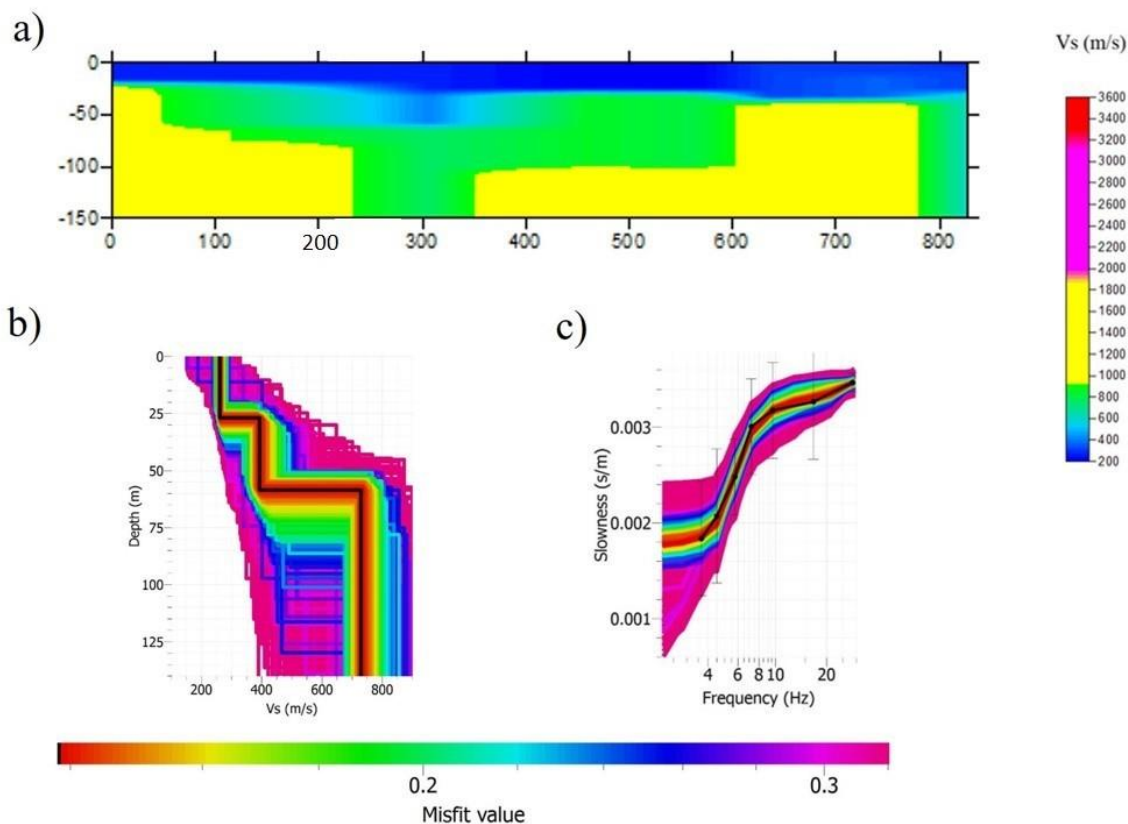


Figure 10: Example of EGFs with the correspondent dispersion curve, obtained from passive seismic data for high-resolution profile shown in Fig. 9: a) EGFs; b) dispersion curve, extracted by MASW technique; c) particle motion diagrams for part of EGF indicated in (a) by red lines.



425

Figure 11: Results of inversion of dispersion curves obtained from passive seismic data of high-resolution XSoDEx profile: a) 2D velocity model obtained by interpolation of 1D velocity models. Velocity color scale is shown in the left. b) an example of 1D velocity model (black line) obtained by inversion of the dispersion curve in (c), corresponding to distance of 200 m in Fig. 11 (a); c) dispersion curve (black line), used for inversion of the velocity model in Fig. 11 (b). Color scale corresponds to values of misfit function during different iteration steps in global optimization algorithm.

430

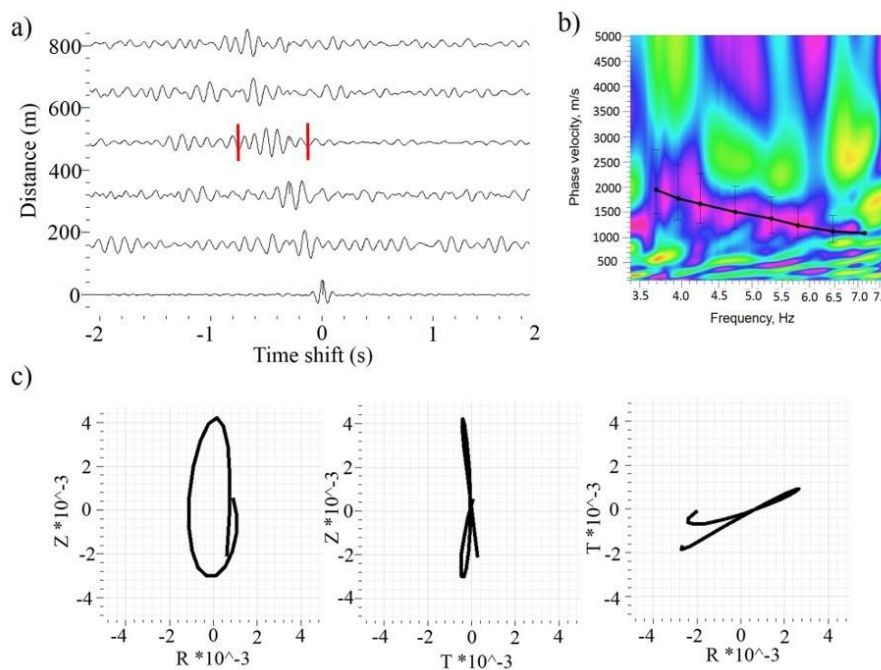


Figure 12: Example of EGFs with correspondent dispersion curve, obtained from passive seismic data: a) EGFs on frequency band 3-8 Hz; b) dispersion curve, calculated from EGFs by MASW technique; c) particle motion diagrams of a surface wave part of an EGF indicated by red lines.

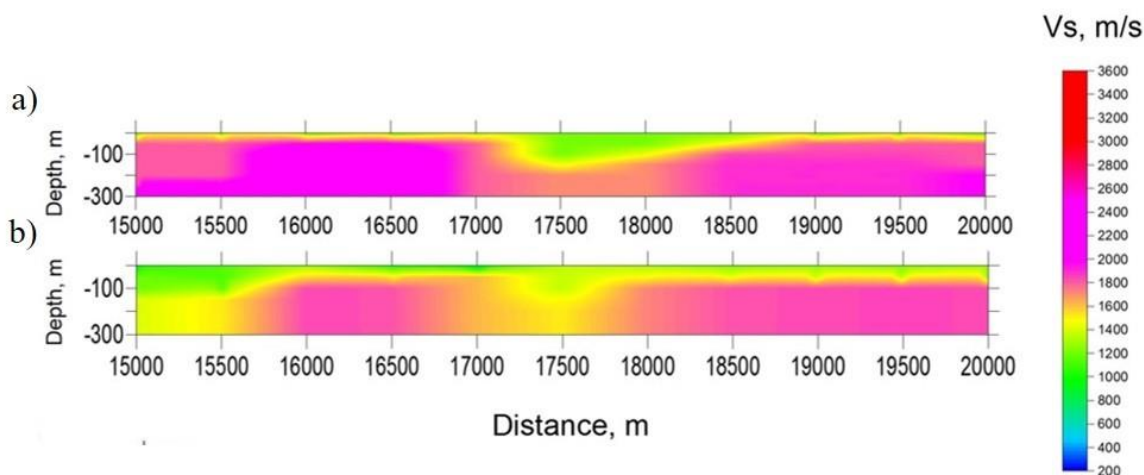
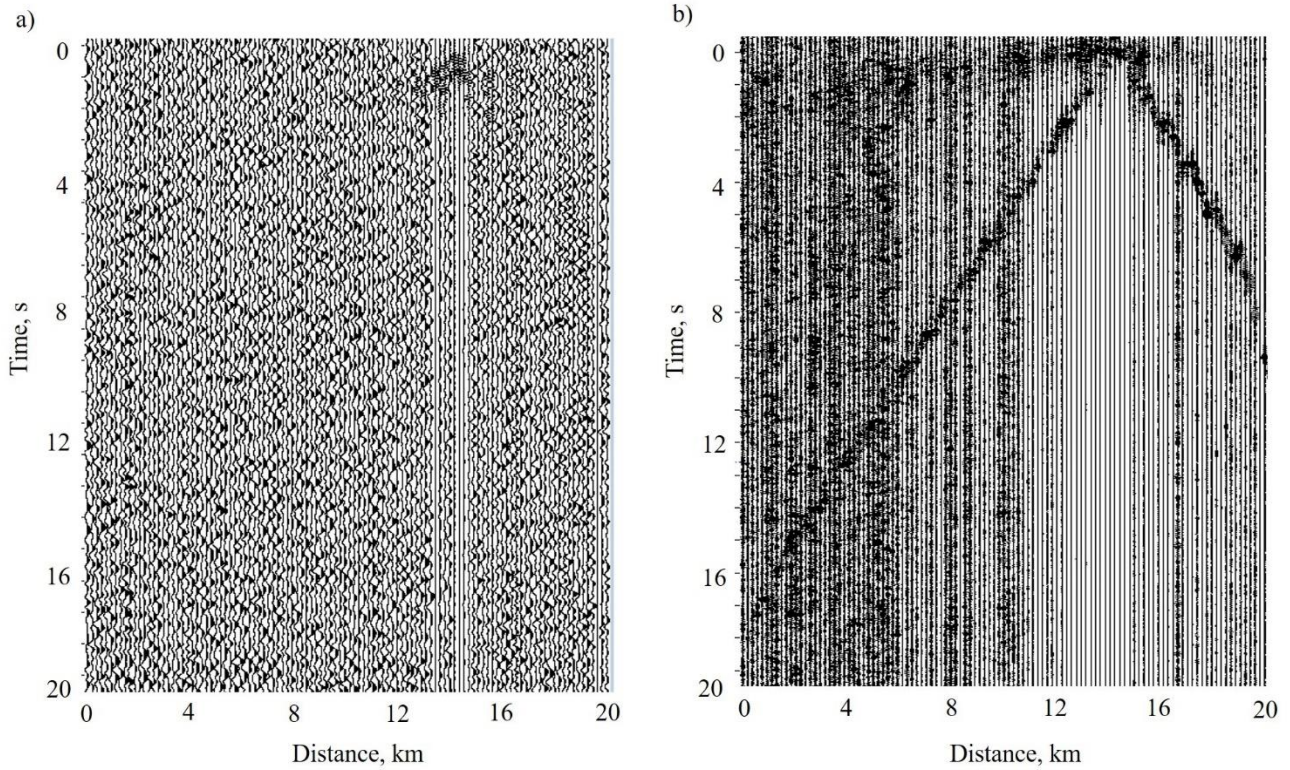
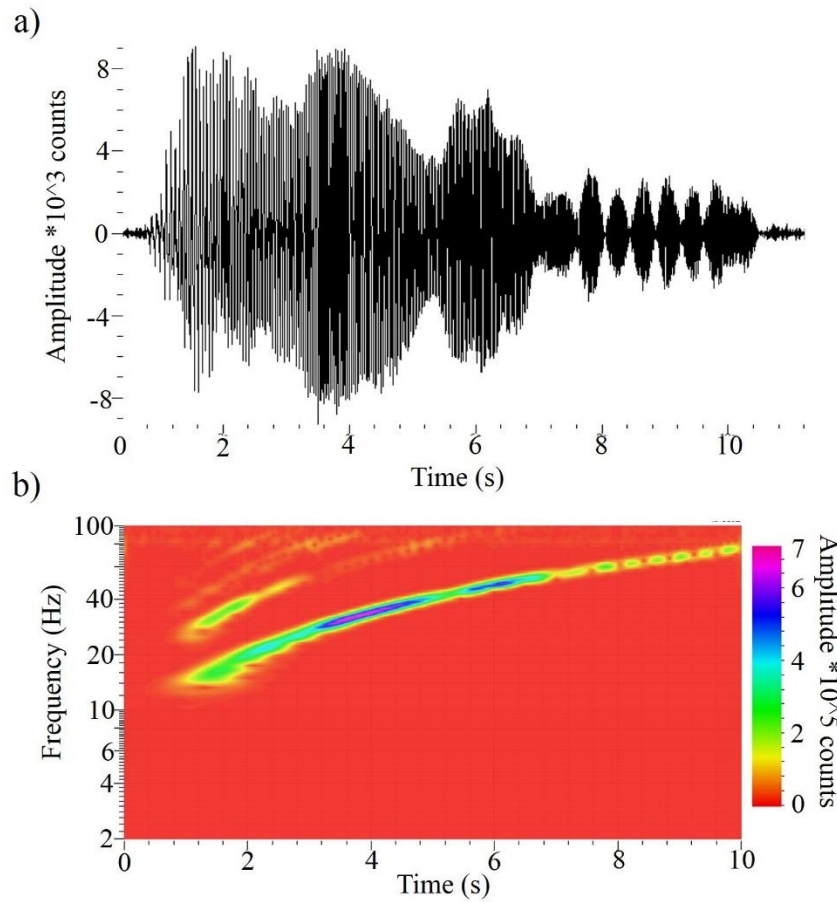


Figure 13: Velocity models calculated by inversion of dispersion curves along the part of Sakatti profile marked by blue in Fig. 9. (a) S-wave velocity model obtained using passive seismic data; (b) S-wave velocity model obtained using controlled-source seismic data.

435



440 **Figure 14: Crosscorrelation functions of signals, produced by Vibroseis© with the data recorded by wireless equipment at large offsets in frequency band of: a) 1-10 Hz, amplitudes normalized at maximum of each trace; b) 20-100 Hz. The signal used for cross correlation is shown in Fig. 15.**



445 **Figure 15: An example of Vibroseis© sweep, recorded by a wireless sensor placed near the vibrator in XSoDEx experiment: a) seismogram; b) spectrogram showing the frequency content of a vibrator signal.**

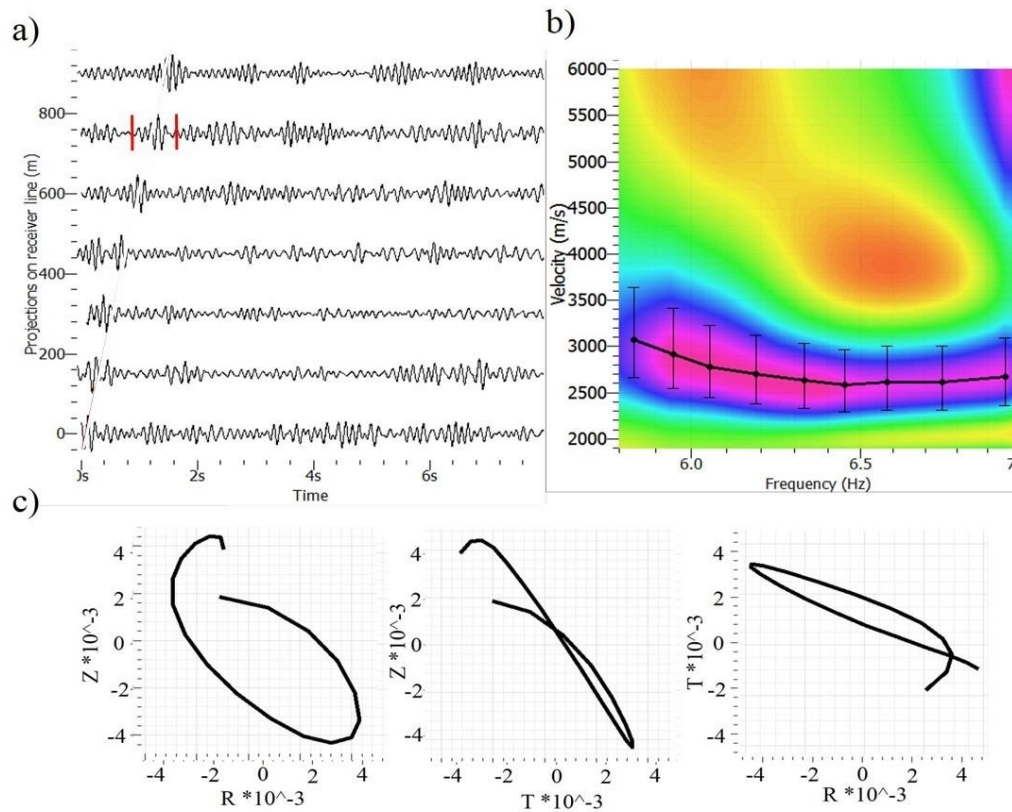
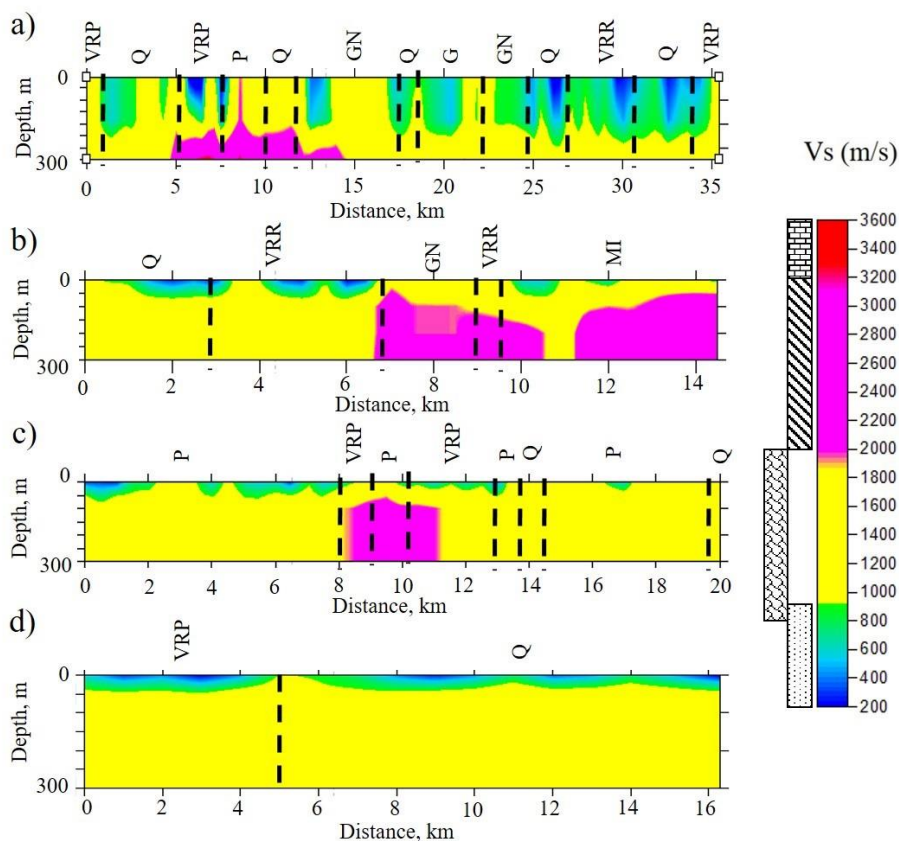


Figure 16: An example of EGFs with correspondent dispersion curve of Rayleigh wave on frequency band 5-10 Hz, obtained by advanced method of passive seismic interferometry: a) EGFs; b) dispersion curve, extracted by MASW technique; c) particle motion diagrams for surface wave part of EGF marked by red in (a).



VRP – volcanic rocks, different types of relatively quartz poor eruption products mainly in Lapland;
 VRR - volcanic rocks, different types of relatively quartz rich eruption products mainly in Lapland;
 Q – quartzite, originally sands deposited in ocean’s shore zone;
 P – paraschist, originally clays deposited at the sea bottom;
 GN – TTG gneiss and magmatite, plutonic rocks related to granite (3500-2750 Ma);
 G – granit;
 MI – layered mafic intrusions, Tornio-Koillismaa belt (2440 Ma).
 - quaternary deposits, coarse-grained sorted sediments;
 - fractured felsic volcanic rocks;
 - fractured mafic and ultramafic volcanic rocks;
 - mafic and ultramafic volcanic rocks.

450

Figure 17: Velocity models, calculated by inversion of dispersion curves, obtained by passive seismic interferometry for XSoDEX profiles shown in Fig. 1. The boundaries of geological units are marked by black dashed lines: a) Pomokairantie; b) Alaliesintie; c) Sakatti; d) Kuusivaarantie.

455